Influence of a bubble curtain on the impact of waves on a vertical wall

O. Kimmoun [1], *A. Ratouis* [2], *L. Brosset* [2]
[1]Ecole Centrale Marseille/IRPHE UMR 7342
Marseille, France
[2]GTT (Gaztransport & Technigaz), Liquid motion dept.
Saint-Rémy-lès-Chevreuse, France

ABSTRACT

Wave impact tests were performed in the flume tank of Ecole Centrale Marseille in order to investigate whether bubble curtains could be a relevant solution as an anti-sloshing device on board membrane LNG carriers for low and partial filling conditions, when associated to a sloshing monitoring system.

Bubble curtains were generated by bubblers located at the foot of the instrumented wall. Parameters related to the wave generation (focalization or solitons) and to the bubblers (type, location and gas flow rate) were screened in order to measure their influence on the impact pressures. The range of gas flow rates studied was restricted to an economically feasible range at full scale.

Whatever the wave generation, the current induced by the bubble curtains favors the overturning of the wave crests and, therefore, accelerates the wave breaking process. The location of the bubblers and the gas flow rate make this process more or less efficient. The variability of the loads is increased and the size of the high loaded areas is reduced. The added compressibility of the aerated water does not seem to be of significant influence.

Depending on the advancement of the wave breaking process for an incident wave, the influence of a bubble curtain on the wave impact loads turns out to be either positive or negative. Consequently, bubble curtains are not considered as a relevant principle for designing an anti-sloshing device on board LNG carriers.

KEY WORDS: sloshing, bubble curtain, hydrodynamic impact, wave impact, flume tank, LNG, compressibility.

INTRODUCTION

Wave impact tests were performed in the wave channel of Ecole Centrale Marseille (ECM) in 2009, at two different scales (see Kimmoun et al., 2010), in order to study the scaling effects on impact pressures. During this campaign, a preparatory work consisted in enabling the generation of deterministic inflow conditions for the wave impacts at both scales. It means that the wave shapes could be repeated very accurately just before the impacts and geometrically-similar shapes could be obtained at both scales. This knowledge makes now the facility very useful for studying the influence of any new parameters on wave impact loads like the structure flexibility, the presence of raised elements on the wall surface or for testing any anti-sloshing device.

This paper presents the results of a new campaign performed in 2010 in ECM, in view to test the ability of bubble curtains to be used as anti-sloshing devices on board LNG carriers, at least for low and medium fill levels, for which impacts are due to breaking waves.

During the 2010 test campaign, wave generation was carried out with a focalization technique, allowing to make the different components of a wave train generated by the wave maker precisely meet at a given location close to the instrumented wall.

As it was considered that the influence of the bubblers with waves induced by a focalization technique could be large but not representative of what would happen with breaking waves generated by ship motions, a second principle for wave generation was considered for the new campaign.

This second principle is based on the generation of solitons running along the tank. A variable bathymetry made possible by a double sloped structure fixed to the tank floor just in front of the wall, made the steepness of the soliton progressively increase until it breaked onto the wall.

After a description of the test set-up, including the two wave generation principles, tests parameters concerning both the wave generation and the bubblers are described. Based on a bibliography study, expected effects of bubble curtains are explained. A sensitivity study allowed to sort out and prioritize the different parameters. Main results are shown. Finally the influence of the bubble curtains on the impact loads for both wave generation principles are presented.

TEST SET-UP

Flume tank

The wave tank is 16.77 m long. A flap-type wave maker is installed at an end of the tank. At the other end, an instrumented vertical wall is located at D = 15.5 m from the wave maker. The longitudinal walls are transparent sections of glass supported by metallic frames. The movable flap and a horizontal bottom lay above the concrete floor of the room.

During the second part of the test campaign, a double sloped structure was fixed to the bottom of the flume, just in front of the wall, in order to create a variable bathymetry. The structure is made of an inclined plane linked to a horizontal plane. **Figure 1** schematically shows the installation and the main proportions.

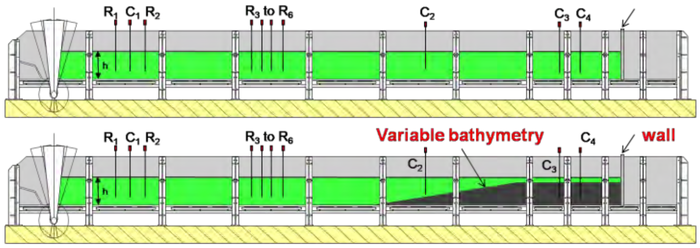

Figure 1 - Schematic description of the wave canal with (bottom) and without (top) the double-sloped floor.

When the flume was used with the flat bottom, the wave generation was carried out with a wave focusing technique. When the flume was used with the inclined bottom structure, only a soliton was generated by the flap.

Wave maker

The wave maker is moved by a hydraulic engine. The flap rotates around a horizontal axis located 40 cm under the raised bottom of the tank. The two principles used for wave generation are presented.

A focusing technique is used to generate a targeted wave elevation *η(x, t)* at given focal distance *x* of the flap and time *t*, from a wave amplitude spectrum *a(ω)*, *ω* being the rotation frequency. The flap rotation signal *θ(x, t)* is deduced from the spectrum thanks to the flap transfer function *C(ω)*.

$$\eta(x,t) = \int_{\omega} a(\omega) e^{i(\omega t - k(\omega)x)}\, d\omega, \theta(x,t) = \int_{\omega} \frac{a(\omega)}{C(\omega)} e^{i(\omega t - k(\omega)x)}\, d\omega$$

The integration of *ω* is discretized on about 65000 equally spaced frequencies. An example of the paddle signal as obtained by focalization is shown in **Figure 2** (left).

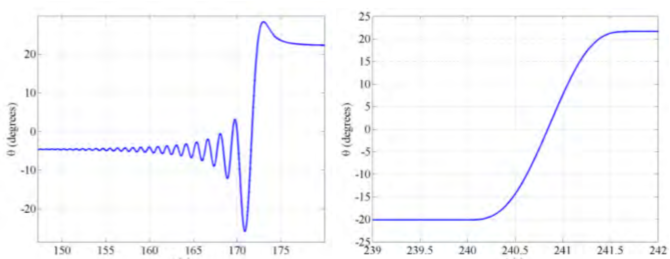

Figure 2 – Paddle signals: (left) space-time focusing, (right) soliton.

A soliton is generated when the double slope beach is used. This soliton corresponds to a second order shallow water paddle solution (Temperville (1985), Guizien and Barthelemy (2002)):

$$X(t) = 2\sqrt{\frac{A'h_0}{3}}\left(1+\frac{A'}{h_0}\right)\tanh(\beta ct/2) + \frac{A'}{3}\sqrt{\frac{3A'}{4h_0}}\frac{\tanh(\beta ct/2)}{\cosh^2(\beta ct/2)}$$

With

$$\beta = \sqrt{\frac{3A'}{h_0^3}}, c = \sqrt{gh_0}\left(1+\frac{A'}{2h_0}+\frac{19A'^2}{40h_0^2}\right) \; and \; \frac{A}{h_0} = \frac{A'}{h_0}\left(1+\frac{5A'}{4h_0}\right)$$

with h_0 the water depth in front of the wave maker and *A* the amplitude of the soliton. An example of the paddle signal as obtained for a soliton generation is shown in **Figure 2** (right).

Optimization of the bathymetry

When running on a positive slope, the steepness of a soliton increases, until the crest overturns. Several parameters contribute to the shape of the soliton: the water depth, the soliton amplitude and the bathymetry.

A double sloped beach was designed with the objective to allow the generation of breaking waves in the flume, for a given range of water depths, taking into account the allowable power of the wave maker. Moreover, the breaking waves had to impact the wall in the area covered by horizontal lines of sensors.

An optimization of the structure geometry was possible using a numerical code developed by Scolan (2010, 2011). The total length of the structure was set at seven meters. The second slope of the structure, adjacent to the impacted wall, was chosen horizontal.

Two parameters have been optimized: the height of the bathymetry along the vertical wall, and the location of the point P, junction of the two planes. The optimization resulted in a height of 0.57 m and a length of the horizontal part of 3 m. Evolution of the calculated free surface shape in these conditions is shown in **Figure 3** and compared to a picture of the real wave obtained by camera 1 (run 181).

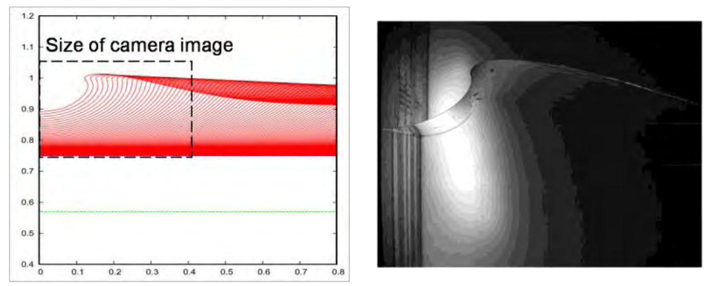

Figure 3 – (Left) Evolution of the calculated free surface for the optimized bathymetry - (Right) Snapshot of the breaking wave in the same conditions (run 181).

Instrumentation

- Six resistive wave gauges referred to as R_1 to R_6 and four capacitive wave gauges referred to as C_1 to C_4 are installed in the canal (see **Figure 1**). The acquisition of the wave gauge signals is triggered by the start of the wave maker. Signals are synchronized.
- 100 PCB pressure transducers are screwed in two metallic modules inserted in the wall. The PCB sensors are piezo-electric. They have a sensitive circular area of 5.5 mm diameter.
- The metallic modules are described in **Figure 4**. They allow sensors arrangements along horizontal and vertical lines with a distance of 1 cm between sensors on the same line and a distance of 5 mm between two parallel lines. Two vertical lines of sensors are set on both modules. Two and six horizontal lines of sensors are set respectively on the left and right modules in the impact zone.
- The data acquisition is performed by a National Instruments PXI system with a sampling frequency at 40 kHz.
- Three high speed cameras are installed close to the end wall, observing the last developments of the breaking waves through the lateral glass wall (see **Figure 5**). The first one allows a general view of the wall and the bubble curtain. A typical picture taken from this camera is shown in **Figure 3** (right). The second and the third allow to check the shape of the waves during the impacts. The picture size of the third camera corresponds to six horizontal lines of pressure sensors. Main parameters of the cameras, as settled for

the tests, are given in **Table 1**.

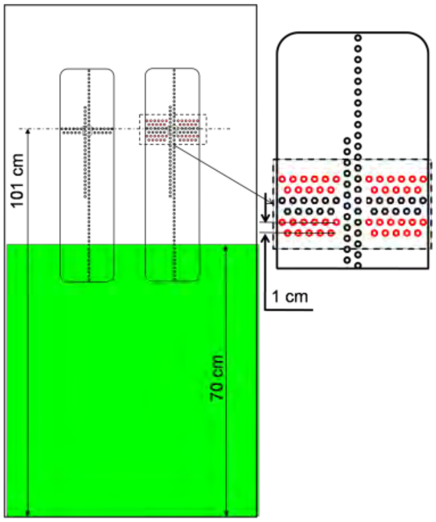

Figure 4 – Test wall and metallic modules for fixation of the pressure sensors.

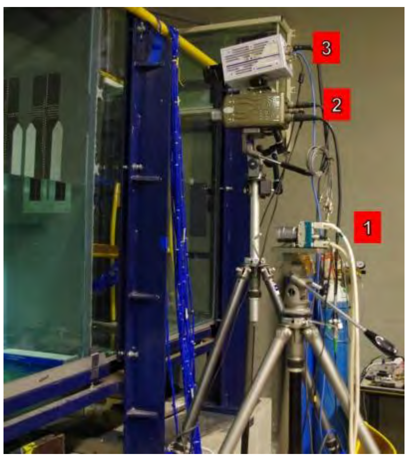

Figure 5 – Side view of the camera set-up. (1) Mikrotron, (2) Phantom and (3) Photron.

Table 1 – Main parameters of the cameras as settled for the tests.

Camera	Frequency (fps)	Resolution (pixels²)	Picture size (cm²)
Mikrotron EOSENS	250	1024x1024	102x102
Vision Research Phantom 7.3	3000	800x600	41.8x31.4
Photron SA2	3000	768x768	13.2x13.2

- The gas used for the bubblers during the tests is oxygen. The gas flow entering into the bubbler is measured by a digital flow meter (model TSI Mass Flowmeter 4140). The sampling frequency is 200 Hz.

TEST PARAMETERS

Wave generation

When the focusing technique was used, eight values of the longitudinal location of the focal point were studied for a constant water depth h=70 cm. They are given in **Table 2**.

Table 2 – Focalization with flat bottom : focal point distance X_f to the flap.

X_f(m)	15.5	15.54	15.56	15.58	15.6	15.65	15.7	15.8	15.9

When a soliton was generated, three amplitudes were studied, given in **Table 3**, combined with different water depths given in **Table 4**.

Table 3 – Generation of soliton with bathymetry : amplitude A of the soliton

A(cm)	19	20	21	23	25	26

Table 4 – Generation of soliton with bathymetry : water depth h

h(cm)	77	77.5	78

Range of gas flow rates (Q_0)

If we ignored any limitation on the gas flow rate insufflated into the bubblers, bubble curtains could already, from the literature, be considered as very efficient anti-sloshing devices (see Laurie (1952), Kurihara (1955-1958)). Indeed, there is always a threshold from which the gas flow rate would reduce dramatically the liquid motions. The real objective of this study is to determine whether sloshing is significantly reduced with the flow rates that could be reached on board LNG carriers, taking into account design and economical constraints.

Therefore, we beforehand need to fix a range of achievable flow rate at full scale and then to convert this range to the flume tank scale.

For the estimation of achievable flow rates at full scale, some assumptions on the operating conditions have to be made. Let us assume that in all tanks of a membrane LNG carrier, single lines of bubblers are installed along the bottom of the lower chamfers. The cumulated length is therefore $L_{fs} = 2.(l_{tank})_{fs} \sim 80$ m for one tank, where fs stands for *full scale*. A continuous running of the system during the voyages would lead to such an amount of gas to feed the bubblers, that the solution is hardly economically conceivable. Therefore, we assume that the anti-sloshing system would be turned on in a given LNG tank, only if sloshing is detected. This supposes that the anti-sloshing device is associated to a sloshing monitoring system. Therefore, the system would be active for relatively short sequences compared to the whole voyage duration.

We assumed a design maximum value for the gas flow rate of Q_{fs}=10 m^3/min for one tank. This design value is to be converted to a maximum flow rate Q_{ms}, where ms stands for *model scale*, for the tests in the laboratory. Obviously the similarity is to be established per length unit. In the lab, the flow rate is delivered by bubblers installed at the foot of the wall. Therefore, the cumulated length to be considered at small scale is $L_{ms} = b_{flume}$, the width of the canal. The following scaling law has been adopted:

$$Q_{ms} = Q_{fs}\,\frac{b_{Flume}}{2l_{Tank}\Lambda}\frac{\Lambda^3}{\sqrt{\Lambda}} \approx 5 \times 10^{-4}\,Q_{fs}$$

Where $\boldsymbol{\Lambda}$ is the geometrical scale considered in the lab, namely 1/6. This allows to establish the range of flow rate to be studied considering that the flow rate at full scale is between 0 and 10 m^3/min. The range of flow rate at small scale is taken accordingly between 0 and 5 l/min.

Table 5 shows the gas flow rates used to feed the bubblers during this study.

Table 5 – Gas flow rate Q_0

Q_0 (l/min)	0.1	0.5	1	2	5

Bubbler types (BT)

During the test campaign, two different bubblers were used. These bubblers correspond to sintered metal tubes manufactured by GKN Sinter with two different pore sizes, respectively 8 (SIKA-R 8 IS, referred to as **R8** or **BT1**) and 100 (SIKA-R 100 IS, referred to as **R100** or **BT2**) microns. The bubblers used during the tests are shown in **Figure 6**.

Thanks to the work of Puleo et al. (2004), we have access to the distribution of bubble sizes (see **Figure 7**) for these two types of bubblers. Results are given for a flow rate of 1 liter/min. R8 produces small bubbles with a maximum probability around 0.25 mm and R100 produces larger bubbles from 1.2 to 2.5mm.

Figure 6 – Bubblers BT1 (left) and BT2 (right) used during the test campaign.

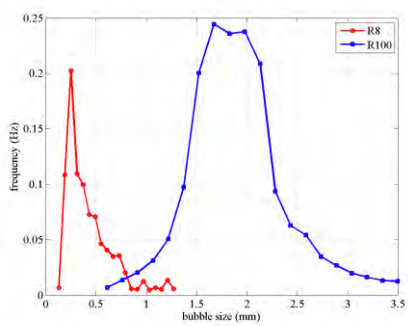

Figure 7 – Bubble size histograms for bubblers used BT1 and BT2.

Typical bubble curtains generated by the three bubblers are presented in **Figure 8**.

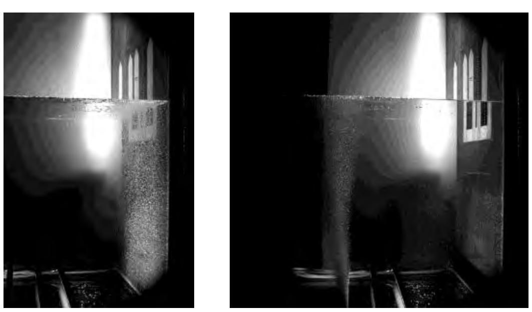

Figure 8 – Bubble Curtains: (left) SIKA-R 100 IS (R100), bubbler position 1 - (right) SIKA-R 8 IS (R8), bubbler position.

Bubbler positions (BP)

The position of the bubblers may influence significantly the efficiency of an anti-sloshing device. To understand the influence of this parameter, four different longitudinal positions were tested referred as BP1 to BP4. Actually, the four locations were tested with the flat bottom and the focusing waves but only two positions were tested with the inclined bottom and the soliton waves (BP1 and BP3). Values are reported in **Table 6**.

Table 6 – Longitudinal positions of the bubblers

Reference	BP1	BP2	BP3	BP4
Distance from the wall (cm)	2.0	28.8	38.7	50.4

For the inclined bottom and the soliton waves cases, the bubblers were placed in cavities inserted within the bottom in order their surfaces were flush with the bottom.

Test matrix

Consequently, the parameters of the study are:

- Wave generation
  - focalization technique :
    - ✓ focal distance (X_f) → **Table 2**
  - generation of a soliton :
    - ✓ amplitude (A) → **Table 3**
    - ✓ water depth (h) → **Table 4**
- Bubblers
    - ✓ bubbler type (BT) → **BT1** (R8), **BT2** (R100)
    - ✓ gas flow rate (Q_0) → **Table 5**
    - ✓ bubbler position (BP) → **Table 6**

Other parameters like the type of gas (Oxygen or Helium), adjuvant added into the water or combinations of two bubblers were also studied but the results are not reported in this paper. A total of 210 runs were performed in order to screen all these parameters with some repetitions of chosen cases.

Tests cases with the focalization technique have mostly been performed with bubbler type BT1 except for a few cases with BT2, exclusively in position BP3.They are defined by a triplet (X_f, Q_0, BP). The different combinations studied are summarized in **Table 7**.

Test cases with generation of a soliton have been performed with bubbler type BT1. They are defined by a triplet (A, h, Q_0). The different combinations studied are summarized in **Table 8**.

Table 7 – Focalization technique – Test cases are defined by (X_f, Q_0, BP). Numbers in Table correspond to bubbler positions (BP). BP=3' corresponds to BP=3 with BT=2, otherwise BT=1.

Q_0 (l/min) **X_f (m)**	**0.1**	**0.5**	**1**	**2**	**5**
15.50	1-2-3	1 to 4-3'	2	1 to 4	2-3-4
15.56					2
15.60	2-3-4	2-3-4-3'		2-3	2-3
15.70	1-2-3	1 to 4-3'		1 to 4-3'	2-3-3'
15.80	1	1	1-3'	3'	3'
15.90			1	1	

Table 8 – Soliton with bubbler type BT1 – Test cases are defined by (A, h, Q_0). Numbers in Table correspond to gas flow rates Q_0 in l/min.

A(cm) **h (cm)**	**19**	**20**	**21**	**23**	**25**	**26**
77		0-3	0-1-3-5	0-3	0-1-3-5	
77.5				0-1-3	0-1-3-5	
78			0-3	0	0-3	0-3-5

EFFECTS OF BUBBLE CURTAINS

The pneumatic breakwater was a popular engineering topic up to the 1960s. The authors from the beginning of the 20^{th} century up to now days (Laurie (1952), Evans (1955), Bulson (1968), Kobus (1968)), agreed that waves are damped by the current and turbulences generated by bubble curtains and that the bubbles themselves have a very small effect on wave damping.

Wave – current interaction

One important effect of the bubble curtain is the generation of a surface current. This surface current takes place over a length that is not easy to define, but which is a few times the order of the depth. The induced flow depends on the bubbler position with regard to the wall. As is shown in **Figure 9**, there are two different cases. When the bubbler is in position 1, all the flow is directed seaward. In comparison, when the bubbler is in position 3 (2 and 4 correspond to the same case as 3), a part of the flow is directed seaward like before and a second part is directed toward the wall, creating a flow cell.

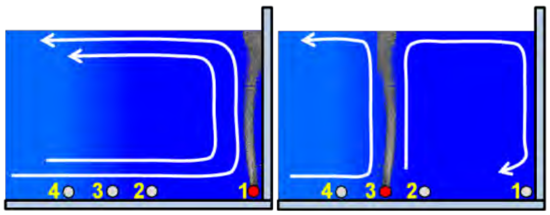

Figure 9 – Typical flows observed, depending on the position of the active bubbler.

This means that the surface current is twice stronger for the bubbler in position 1 than in others positions. This current has two effects on waves. The first is the modification of the wave number and the celerity (Doppler effect). For a current U, opposite to the waves, the dispersion relation is modified:

$$(\omega + kU)^2 = gk\tanh(kh)$$

With k the wave vector, ω the pulsation and h the depth. The second effect is a shoaling effect and from a given frequency, the wave blocking. Such opposite current slows down the wave leading to an increase of the wave steepness, which sometimes leads to wave breaking. The wave is blocked when the current is strong enough to prevent the wave energy from traveling upstream. That is when the group velocity C_g goes to zero. The problem in the case of a bubble curtain is to determine the surface current. There is no exact solution for this problem, but there are many approximate solutions. Bulson (1959) studied the theory and design of bubble or pneumatic breakwater. From analytical and experimental studies carried out by the author and others, design formulae are obtained. The surface velocity U, is given by:

$$U = 1.46\sqrt[3]{\frac{\rho g p_a Q_0}{p_a + \rho g d}}$$

with p_a the atmospheric pressure and d the depth of the bubbler. Even if this solution is not very accurate, it is enough to understand our results. For the air flow rates tested during the experiment from 0.1 to 5 liters/min, the range of U is from 4.2 to 11.4 cm/s. Using these values of U, the relative modification of the phase velocity is plotted in **Figure 10**, with c the phase velocity with a given current U, and c_0 the phase velocity without current. It is clear from this figure that the induced surface current implies a defocusing of the wave group. For the current corresponding to Q_0=5 l/min, the wave blocking can be observed for frequency greater than 2.5 Hz.

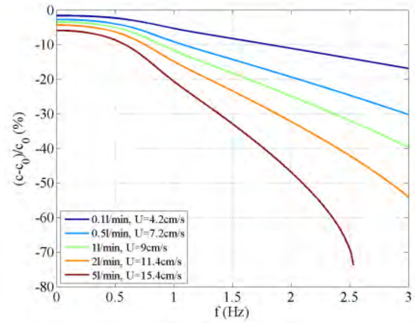

Figure 10 – relative modification of the phase velocity due to the induced surface current.

Wave dissipation

Preissler (1960) established a semi-empirical law for the problem of waves passing through a bubbles curtain. This relation gives the air flow rates as function of the wave dissipation:

$$Q_0 = 1.56\,10^{-4}(200-p)p\frac{H_I^2\sqrt{\lambda}}{2nD}\left(1+\frac{2kh}{\sinh(2kh)}\sqrt{\tanh(kh)}\right)$$

Where p is the wave height decay ratio and equal to $100(H_I-H_T)/H_I$, in which H_I is the incident wave height and H_T is the transmitted wave height. λ is the wavelength and k the corresponding wave number, h is the water depth and D is depth of the bubbler. n corresponds to the wave damping efficiency and is always less than one. From this relation, it is possible to calculate, for a given flow rate, the efficiency in terms of wave height ratio H_T/H_I as a function of wavelength (and the frequency). This relation was chosen for the good agreement with the Kurihara's experiments (Hensen, 1957). To estimate n, we used the experiments of Zhang et al. (2010). In these experiments, the wave transmission for different flow rates, wave amplitudes and periods were measured. Using the Preissler formula, values of n are calculated and a mean value is found and equal to 0.4.

Figure 11 displayed the ratio of the transmitted to the incident wave height, for the different air flow rates (i.e. 0.1, 0.5, 1, 2 and 5 l/min). The bubble curtain acts as a low-pass filter. Indeed, the major part of the energy of the wave group is not affected by dissipation, but the high frequency components are partly or completely dissipated. The effect of this filter on the focusing wave is not straightforward and is always combined with the modification of the phase velocity described before. Nevertheless, this effect participates to the disorganization of the wave group.

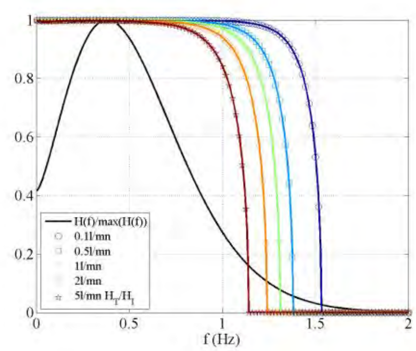

Figure 11 – Ratio of the transmitted to the incident wave height as a function of the frequency for the air flow rates performed during the experiment. The black curve corresponds to the amplitude distribution of the focusing wave.

Vertical location of the wave impact

During the experiments when performed without air flow, the wave amplitude was adjusted to obtain the crest impact on the middle of the six horizontal lines of pressure sensors (see **Figure 4**). It turned out that, the position of the crest during the impact was modified by the airflow and the longitudinal location of the focal point of the wave group was also changed, modifying therefore the size of the entrapped gas pocket. By adjusting the focal distance, it was possible to obtain again the same gas pocket size as without air flow. The main difference was an increase of the vertical location of the crest during the impact as shown in **Figure 12**.

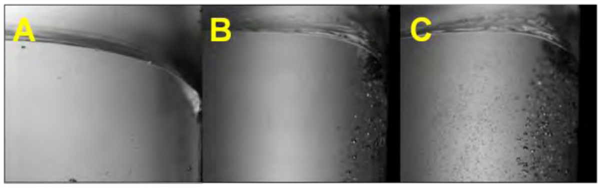

Figure 12 – Wave focusing cases. Modification of the focal distance to obtain a "flip-through" case, with increasing air flow rates. BP1, (A) X_f =15.60m, (B) X_f =15.9 m, Q_0=1.5 l/min, (C) X_f =16.2 m, Q_0=5 l/min.

This modification of the impact location is also visible, looking to the spatial distribution of pressure as shown in **Figure 13**. For the test (C), the vertical position of the impact was at the limit of the sensor area.

This effect was also present for the soliton waves.

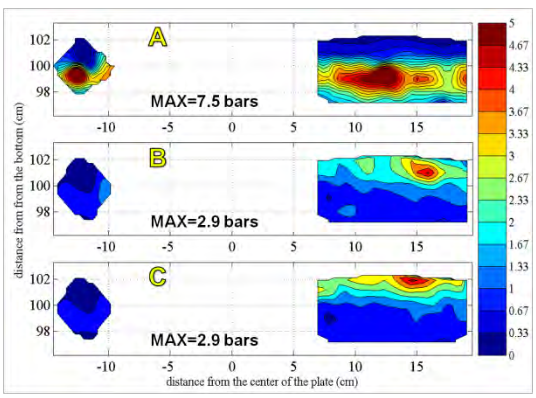

Figure 13 – Spatial distributions of the recorded pressures at time of maximum pressure for the cases presented in **Figure 12.**

Turbulence – instability of the wave crest

The bubble curtain, in addition to the effect of damping and phase lag, has also an influence on the regularity of the wave crest. The two examples display in **Figure 14**(B and C), a small air flow rate of 1 liter/min for a bubbler in position 1, show clearly disturbances on the crest line. These disturbances could lead to a pressure decrease, as has often been observed. But it, sometimes, has an opposite effect as shown in **Figure 15**.

For the case without air flow, the maximum pressure is about 7 bars with an almost homogeneous horizontal distribution. For the cases with air flow, the maximum pressure is respectively equal to 9 and 11.5 bars. The distribution of pressure is less homogeneous in these cases and pressure maximum is located on a small spot.

Figure 14 – Bubble curtain effect on free surface roughness and crest instabilities – (A) no air flow, X_f =15.60m and (B and C) Q_0=1 l/min, X_f =15.80 m, BP1, BT1.

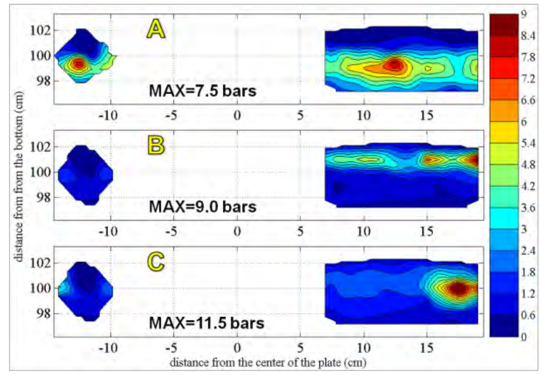

Figure 15 – Spatial distribution of the pressures for the three cases presented in **Figure 14**.

Aeration and compressibility of water

Compressibility and density of the liquid phase are of full importance for the impact characteristics. We can consider that the curtain has a homogeneous compressibility and a density different than those of pure water. To evaluate how those properties are changed with the presence of bubbles, an estimation of the void fraction is needed. Estimations of bubbles velocities and size of curtain are necessary for the estimation of the void fraction.

Thanks to the PIV (Particle Image Velocimetry) algorithm, it is possible to evaluate the velocities in the bubble curtain. In that case, the bubbles replace the particles. Pictures from the Mikrotron camera are used. The sample frequency for this camera is 250 Hz and pixel size is 1 mm. In **Figure 16**, velocity maps for the bubbler position BP3, the bubbler type BT1 and air flow rates ranging from Q_0=0.5 l/min to 5 l/min are displayed. **Figure 17**, presents the same cases but for the bubbler type BT2. Velocity maps have been calculated for five hundred couples of image and for 3 different air flow rates Q_0=0.5, 2, 5 l/min.

From this data the average vertical velocity $v(z)$ is calculated for the two bubbler types (**Figures 18** and **Figures 19**). For the bubbler BT1, the velocity increases with the air flow rate. This means that the size of the bubbles increases also with the air flow rate, while the dependence with the air flow rate for the bubbler BT2 is less pronounced. Due to the larger porosity, the bubble size remains the same for the different flow rates tested during the experiments. **Table 9** gives the mean vertical velocities.

Table 9 – Mean vertical velocities for BT1 and BT2

Q_0 (l/min)	0.5	2	5
BT1, mean $V(z)$ (cm/s)	26	33	39
BT2, mean $V(z)$ (cm/s)	33	34	40

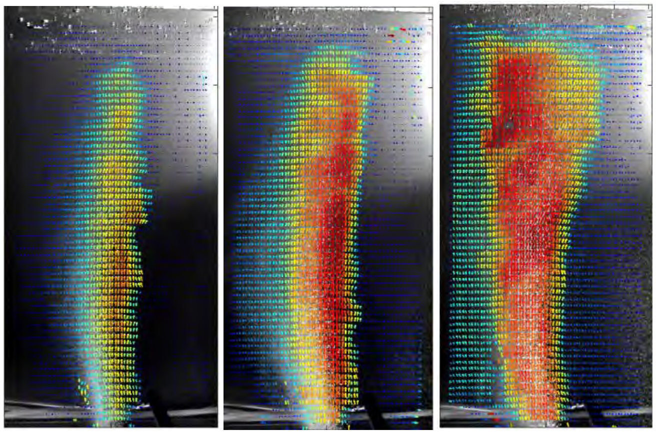

Figure 16 – velocity map for BP3, BT1, and for Q_0 in l/min (left) 0.5, (middle) 2 and (right) 5. The red color corresponds to 50 cm/s.

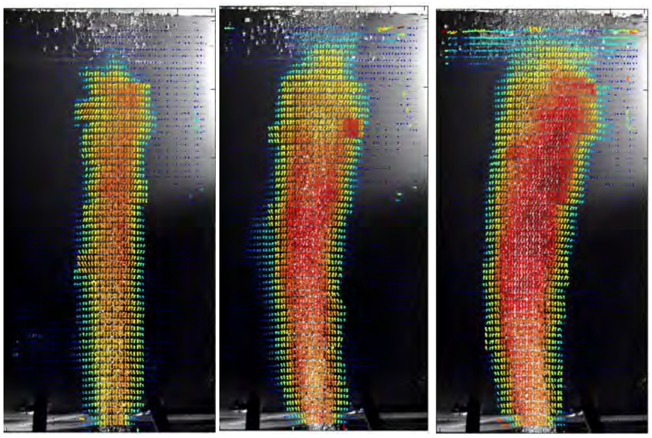

Figure 17 – same as **Figure 16** for BT2.

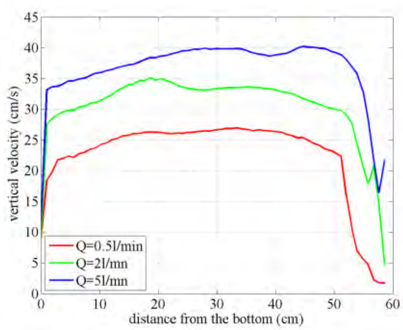

Figure 18 – Evolution of the mean vertical velocity along the vertical, for the cases corresponding to **Figure 16** (BP3, BT1, and for Q_0 in l/min (left) 0.5, (middle) 2 and (right) 5).

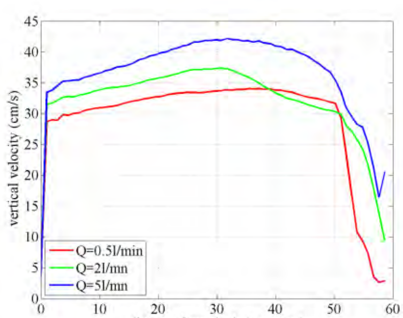

Figure 19 – Same as **Figure 18** for BT2, corresponding to **Figure 17**

Thanks to the velocity profile it is possible to estimate the width of the bubble curtain. If the width of the bubble curtain *b(z)* is known for every vertical position, then the void fraction can be estimated as :

$$\alpha(z) = \frac{Q_0}{L\, v(z)\, b(z)}$$

with L the width of the tank.

From Brennen (1995), it is possible to estimate the speed of sound in water:

$$c = \left((\rho_w(1-\alpha) + \rho_a\alpha) \left[\frac{\alpha}{np} + \frac{1-\alpha}{K_1} \right] \right)^{1/2}$$

With ρ_w the water density, ρ_a the air density, n the isothermal polytropic index (n=1), p the pressure and K_1 the bulk modulus of water.

The void fraction and the corresponding speed of sound are presented in **Figure 20**, for the bubbler BT2 in position BP3 and flow rates 0.5, 2, 5 l/min.

The void fraction shows very small values ranging from 0.8% near the bubbler to 0.3% near the free surface. These low values are nevertheless sufficient to drastically reduce the speed of sound in the liquid phase from 1500 to 150 m/s near the surface, for the largest fraction of air. As the compressibility is directly related to the speed of sound, the compressibility of the water and oxygen mixture is theoretically significantly changed when bubbles are introduced.

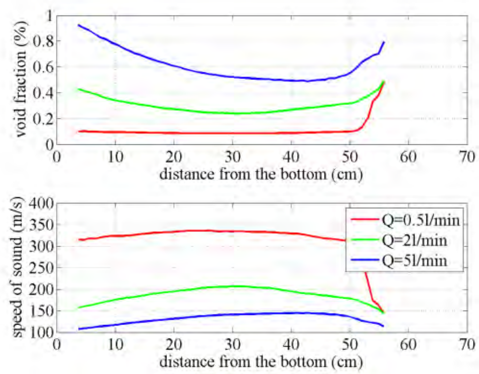

Figure 20 – Vertical evolution for different flow rates of (up) the void fraction, (down) the speed of sound with BP3 and BT2.

It can be noticed that the air fraction in the crest should be of the same order as the values found near the surface before the arrival of the wave, because the bubble curtain was advected by the wave, as seen previously.

SENSITIVITY STUDIES

Influence of the bubble air flow rate on the wave group focusing

For a same focal distance X_f = 15.60 m, a same bubbler type (BT1) and position (BP2), the evolutions of the wave shape are displayed in **Figure 21**, as function of the air flow rates (from 0 to 5 l/min). These pictures come from the Photron camera, and the real size of the pictures is 13.2x13.2 cm². We observe that the air flow implies first, a defocusing of the wave group (the focal distance seems to decrease and therefore the wave breaks earlier) and secondly, a perturbation of the wave crest. The bubble curtain is advected by the wave and is entrapped in the crest during the impact.

The maximum pressures for these cases are reported in **Table 10**. The maximum pressure seems to decrease when the gas flow rate increases.

Table 10 – Influence of the air flow rate on the maximum pressure

Q_0 (l/min)	0	0.1	0.5	2	5
Max pressure (bars)	5.5	2.4	1.41	1.2	0.9

The second case, shown in **Figure 22**, corresponds to bubbler type BT1 with bubbler position BP1. Test (A) without air flow corresponds to a slosh case, when the focal distance is behind the wall.

As for the previous cases, we observe a defocusing of the wave group, with a focal point distance which decreases for increasing air flow. The corresponding maximum pressures are reported in **Table 11**.

In this case, a small flow rate (0.1 l/min), is enough to create a small gas pocket, and thus produce high pressure. By increasing further the gas flow rate, the size of the gas pocket increases and the pressure decreases.

Table 11 – Influence of the air flow rate on the maximum pressures

Q_0 (l/min)	0	0.1	0.5	2
Max pressure (bars)	0.6	3.2	1.0	0.9

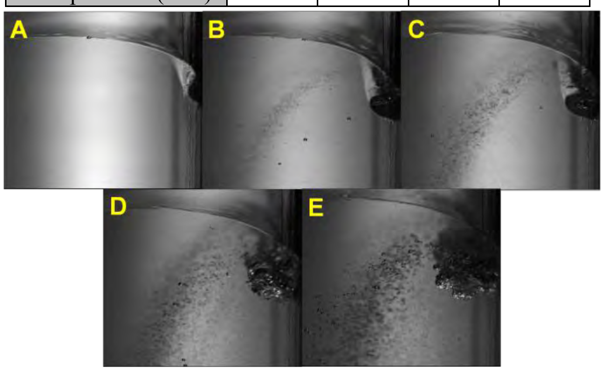

Figure 21 – Wave focusing cases. Focal distance X_f=15.60 m, BT1, BP2, Q_0 in liters/min, (A) 0, (B) 0.1, (C) 0.5, (D) 2 and (E) 5.

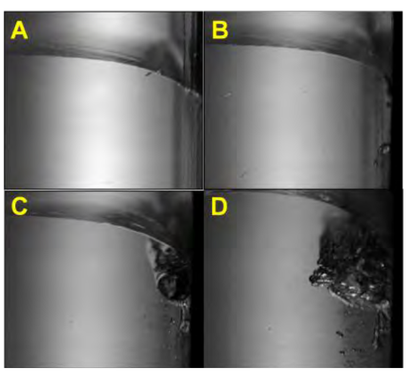

Figure 22 – Wave focusing cases. Influence of the air flow rates. BT1, BP1, X_f =15.7 m, Q_0 in liters/min (A) 0, (B) 0.1, (C) 0.5, (D) 2.

The bubble flow favors the breaking process. This might lead to a reduction of impact pressures when this makes prevent the generation of a flip-through. On the contrary this could generate flip-throughs and therefore high pressures when mild slosh impacts would have normally occurred.

Influence of the bubbler type : BT1 versus BT2

Table 9 displayed the mean vertical velocity in the bubble curtain for both types of bubblers. For the larger flow rates (i.e. greater than 2 l/min), the mean values are almost the same for both tested bubblers. The main differences are for the smaller flow rate (i.e. 0.5 l/min), where the mean velocity for BT1 is 26 cm/s and 33 cm/s for BT2. Because the velocity is directly related to the mean bubble size, this means that bubbles are larger in the case of BT2. This behavior is expected since the porosity of BT1 is smaller. However when the flow rate is larger, the mean bubble size of the two bubblers seems to converge.

Figure 23 shows the comparison between the pressure maps obtained with both bubblers for the same initial conditions. Even if the pressure distribution is not exactly the same, the shape of the crest and the type of impact are very similar. Small differences can be observed on pictures, with larger bubbles size for the bubbler BT2. However, this difference has little influence on the impact. This behavior is confirmed by the other tests and the maximum pressures are always of the same order.

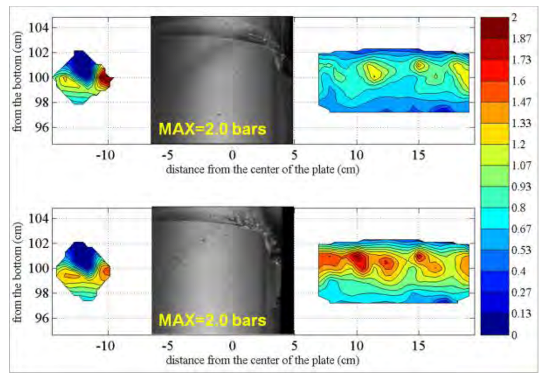

Figure 23 – Wave focusing cases. Influence of the bubbler type. BP3, X_f =15.6 m, Q_0=0.5 l/min (Top) BT1, (Bottom) BT2.

Influence of the parameters of the Soliton generation

For the study with the variable bathymetry, two parameters are used to modify the type of impact, the amplitude of the wave and the water depth.

The influence of the water depth is illustrated by a first example presented in **Figure 24.** The ampitude of the soliton is kept constant for three different water depths. The wave starts breaking later and the vertical position of impact is hihger for larger depth. This behaviour is highlited in **Figure 25** showing the pressure map on the wall for the three waves.

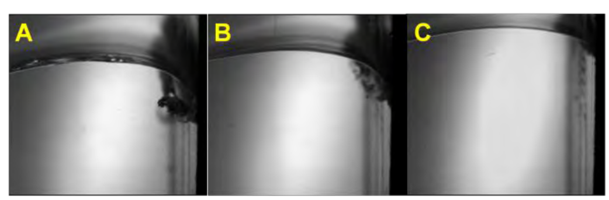

Figure 24 – Soliton cases. Influence of the water depth. A=23 cm, (A) h=77 cm, (B) h=77.5 cm, (C) h=78 cm.

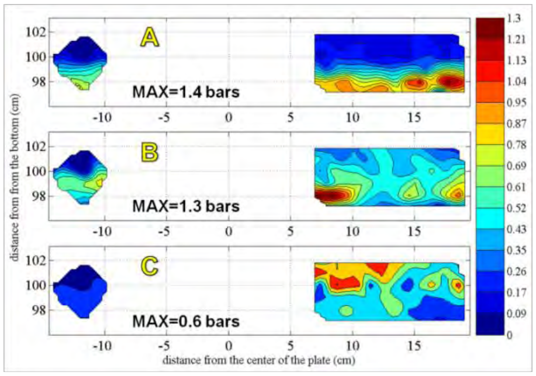

Figure 25 – Pressure distribution for the three cases in **Figure 24**.

The influence of the soliton amplitude is illustrated by a second example presented in **Figure 26.** Three different amplitudes of the soliton, ranging from 23 to 26 cm, are studied for the same water depth. The wave starts breaking earlier for larger amplitudes of the soliton and the vertical location of the crest impact is lower. This behavior is confirmed by the pressure map for the three waves shown in **Figure 27**. Finally, these two examples showed that it is possible to tune the two parameters in order to adjust the location of the crest impact.

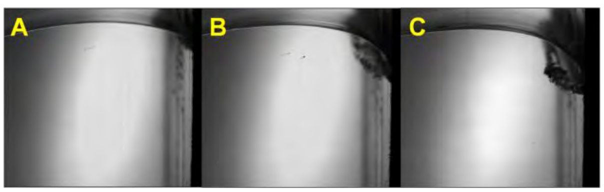

Figure 26 – Soliton cases. Influence of amplitude. h=0.78m, (A) A=23cm, (B) A=25cm, (C) A=26cm

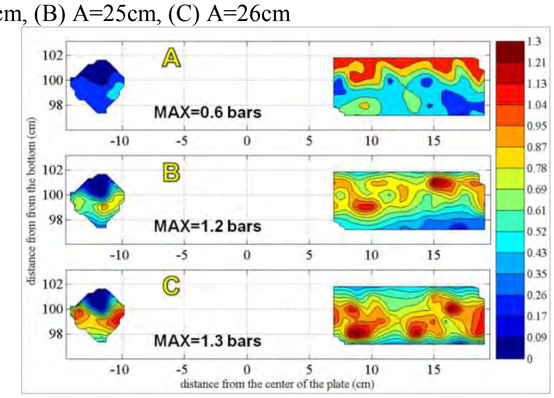

Figure 27 – Pressure distribution for the cases of **Figure 26**.

The variability of the impact pressure measurement when wave inflow conditions are accurately repeated has also been studied. One of the reasons to perform experiments with the soliton was to obtain the simplest waves in order to achieve the best repeatability of the pressure measurements at the crest level (the repeatability of the pressure measurements within the gas pocket is easy to achieve). Unfortunately the wave crest is subjected to a free surface instability, just before impact, mainly due to the flow of escaping air when the crest approaches the wall. This instability, referred to as Kelvin-Helmhotz instability (see Drazin, 2004), leads to inhomogeneities in the pressure distribution. It is considered as the main cause for pressure variability for liquid impacts and it has also been shown that it appears differently at different scales, likely due to surface tension (see Lafeber, 2012).

The conditions that led to the wave shown in **Figure 26(B)** has been repeated another time. Both wave shapes and the pressure map for the second wave are shown in **Figure 28**. Pressure maps for both cases can therefore be compared by looking at **Figure 27(B)** and **Figure 28**. For the same initial conditions, although we succeeded to repeat accurately the same shape of breaking wave, a maximum pressure of 1.2 bars was obtained in the first case while a maximum pressure of 4 bars was obtained in the second case.

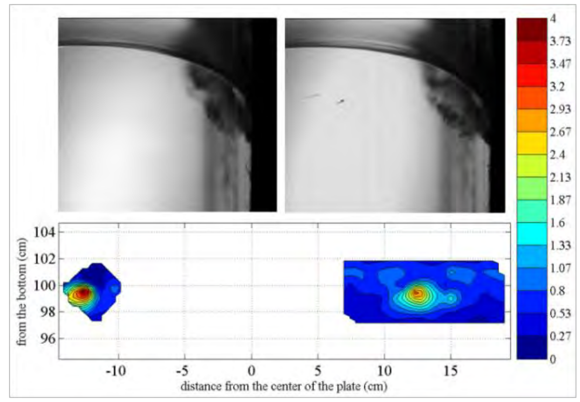

Figure 28 – Soliton cases. Comparison between two same initial conditions. h=0.78 m, A=25 cm, (Top-left) wave presented in **Figure 26(B)** and **Figure 27(B)**, (Top-right) wave obtained by repetition of the same condition, (Bottom) pressure map for the second wave.

To understand the relative influence on the wave impacts between either the gas flow rates from the bubblers or the spoiling effect of the escaping air flow described above, two examples are presented. The first example corresponds to the bubbler position BP3. Three tests are presented in **Figure 29**, for air flow rates respectively equal to 0, 1 and 3 liters/min. At first glance, the wave shape is very similar in all three cases. But the gas pocket seems retained by the bubble curtain and, the larger the air flow, the further the gas pocket from the wall. This trend is observed for the other tests with the bubbler position BP3. This difference in the wave shapes leads to only small differences on the pressures as shown in **Figure 30**.

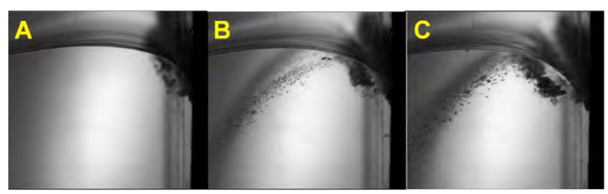

Figure 29 – Soliton cases. Influence of the air flow rates. BP3, A=23 cm, h=77.5 cm, (A) Q_0=0, (B), Q_0=1 l/min, (C) Q_0=3 l/min

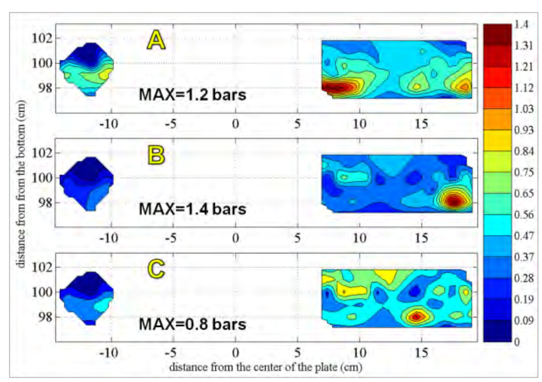

Figure 30 – Pressure distribution for the three cases of **Figure 29**.

The second example corresponds to the bubbler position BP1. Three waves are presented in **Figure 31**, for air flow rates respectively equal to 0, 1 and 3 liters/min. As in the previous cases with bubbler position BP3, the shape of the waves remains globally the same. The differences come from the shape of the gas pocket and more particularly from the lower and the left parts of the pocket. The higher the flow rate, the larger the bottom of the pocket shifts down, and the left size of the pocket nears the wall. But finally, the size of the gas pocket remains approximately the same, with the same frequency of oscillations and maximum for the pressure signals, as shown in **Figure 32**.

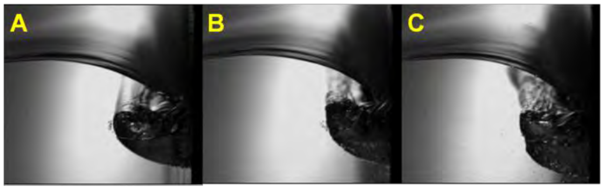

Figure 31 – Soliton cases. Influence of the air flow rates. BP1, A=25 cm, h=77 cm, (A) Q_0=0, (B), Q_0=1 l/min, (C), Q_0=3 l/min.

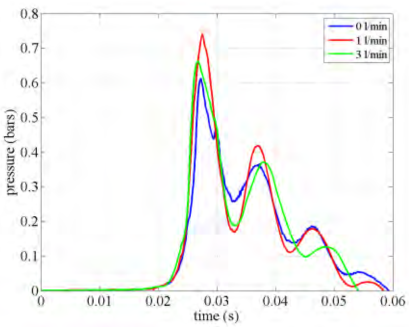

Figure 32 – Soliton cases. Time traces of the pressure sensor corresponding to the maximum pressure for the cases presented in **Figure 31**.

So, finally it is believed that the flow rate of bubbles has less influence on the wave shape and on the impact pressures when the breaking wave is generated by a soliton with a given bathymetry than when the breaking wave is generated by a focalization technique. In the first case, the influence is likely hidden by the spoiling variability of the pressure measurements due to Kelvin-Helmholtz instability of the free surface induced by the escaping gas flow during the wave approach.

INFLUENCE OF THE BUBBLERS ON LOCAL PRESSURES AND FORCES

Impact waves generated by focalization

To understand the efficiency of such device, a global analysis is needed. As the differences between the results with bubblers BT1 and BT2 are small, only results for BT1 are presented.

Figure 33 shows the evolution of the maximum pressure as function of the focal distance and the air flow rate in the bubblers. The bubbler position is BP1. Without air flow, the classical behavior for this kind of wave group is found. The small focal distances (<15.5 m) correspond to gas-pocket kind of impacts, leading to relatively small pressure. When this distance is larger, the gas pocket becomes smaller, and the pressure larger, up to the case (around 15.58) where the gas pocket disappears, the "flip-through" case, leading to the maximum pressures (here around 6-7 bars). For the "flip-through" cases, the spreading of the maximum pressure measurement is high for accurate repetitions of the steering signal of the wave maker. Here, maximum pressures vary between 2 and 7 bars. Flip-Through impact corresponds to the sharp transition between waves with and without gas pocket. If the focal distance keeps increasing, the gas pocket disappears completely. These cases called "slosh"waves lead always to small pressures.

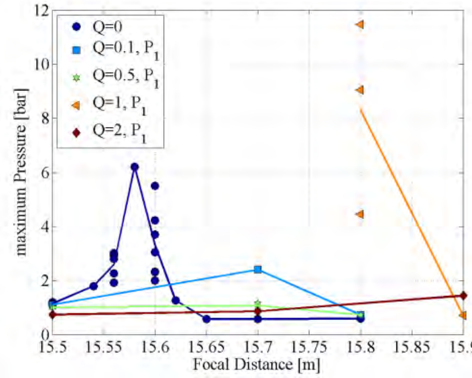

Figure 33 – Focusing case - Evolution of the maximum pressure as a function of focal distance and bubbler air flow rate. Bubbler position BP1.

For the cases with bubbles, two behaviors can be distinguished. The cases for Q_0 equal to 0.1, 0.5 and 2 liters/min, for which the maximum pressure decrease with lower values at 2.2 bars, and the case for Q_0 equal to 1 liter/min, for which the maximum pressure reaches values greater than 8 bars (9 and 11.5 bars).

These two last tests were already presented as cases (B) and (C) in **Figures 14** and **Figure 15**. As it was already noticed, they correspond to an adjustment of the focal distance to obtain a "flip-through" case with bubbles. The main difference with the Flip-Through case without bubbles is due to instabilities of the crest presented in the paragraph "*Turbulence – instability of the wave crest*". These instabilities can lead to high pressures but very localized in space.

To get an idea of the global distribution of the impact pressure, it is interesting to calculate the force acting on the area defined by the pressure sensor array. This area, shown on the figures representing a pressure distribution (e.g. **Figure 30**), represents a surface S equal to 70 cm^2. The force is calculated for each time step and the maximum force is deduced.

$$F(t) = \int_S p(t, M) dS, \;\; F_{max} = max(F(t))$$

Figure 34 is equivalent to **Figure 33**, but for the maximum forces instead of local pressures. The maximum is found for the case without flow. The maximum force is 1250 N. While the wave for Q_0=1 l/min and X_f=15.80 m corresponds to the strongest local pressures, the inhomogeneous nature of the pressure distribution leads to smaller forces than what would be expected. The bubble curtain acts as a system that mitigates the overall load, but may increase local pressure.

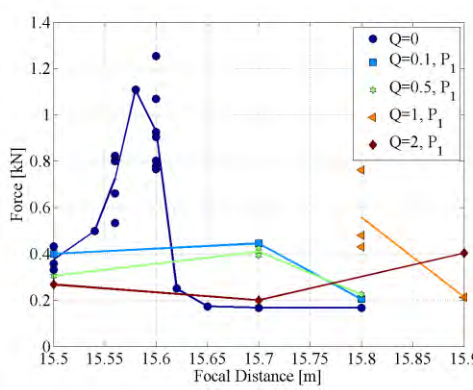

Figure 34 – Focusing case, Evolution of the maximum force as a function of focal distance and air flow rate. Bubbler position BP1.

Results for bubbler positions BP2, BP3 or BP4 are very similar. Hence, for the sake of conciseness, only results for BP3 are presented below. **Figure 35** is similar to **Figure 34** but for BP3 instead of BP1. For this position of the bubbler, it was more difficult to find a focal distance to re-obtain a "flip-through" impact.

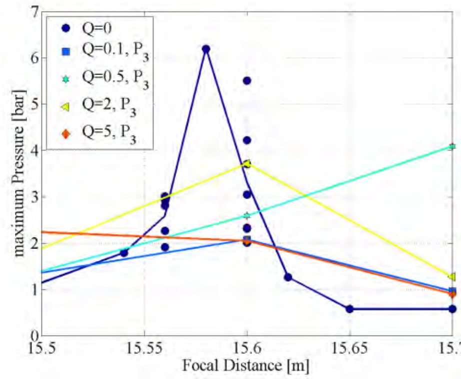

Figure 35 – Focusing case, Evolution of the maximum pressure as a function of focal distance and bubbler air flow rate. Bubbler position BP3.

However, two tests led to high pressures (> 3 bars) : the test with Q_0=0.5 l/min and X_f=15.7 m and the test with Q_0=2 l/min and X_f=15.60 m. In the first case, the high pressure spot is very localized and is located in the upper right area of the pressure array. It is likely that higher pressures occurred above this area but could not be recorded. This bias did not happen with the second case with a pressure hot spot much more centered with regard to the sensor array.

Therefore, due to the localized nature of the impact pressures when bubble curtains are present, the forces presented in **Figure 36** show small intensities for all the cases with air flow.

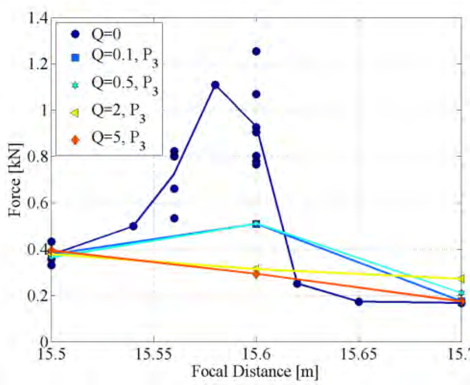

Figure 36 – Focusing case, Evolution of the maximum force as a function of focal distance and air flow rate. Bubbler position BP3.

Conclusions are the same as for bubbler position BP1: bubble curtains are efficient to reduce the overall load (force) but not to prevent high local pressures.

Impact waves generated by a soliton and a variable bathymetry

For the soliton and variable bathymetry, results will first be shown for cases without bubbles. **Figure 37** shows the maximum pressure recorded as a function of the soliton amplitude for the different water depths.

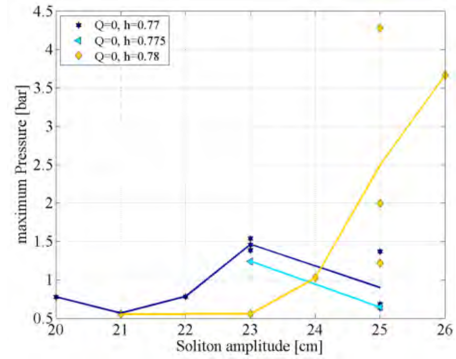

Figure 37 – Soliton cases, evolution of the maximum pressure as a function of the soliton amplitude and the water depth.

For the water depth h=77 cm, the maximum pressure first increases when the amplitude increases until a maximum around A=23 cm. For larger amplitudes the maximum pressure decreases. This corresponds to the evolution of wave impact types from the gas-pocket wave impact, to the "flip-through" for the maximal pressures and finally the "slosh" wave impact. In comparison with the focusing technique, the measured pressures remain relatively small.

For h=0.775m, the behavior seems to be the same but there is a lack of available data (only two waves tested). The water depth h=0.78m shows also the general trends with Flip-Through conditions for a larger amplitude (A=25 cm) than for smaller depth, with a large spreading of the peak pressures when the same condition is repeated.

To illustrate this spreading, the three runs corresponding to the highest pressures (for A=25 cm and A=26 cm) are presented in **Figure 38** (wave shapes) and **Figure 39** (maximum pressure map).

The differences on the wave shapes are very small, especially for cases of the same amplitude, while for these cases the maximum pressure increased from 2 to 4.3 bars. As for the focusing technique, the crest is subjected to free surface instabilities, leading to very localized pressure peaks, even without bubbles.

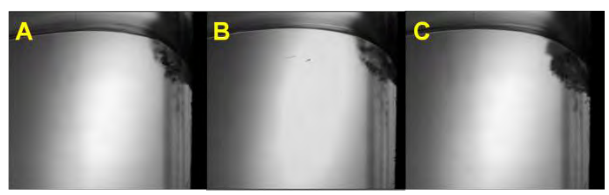

Figure 38 – Soliton cases, h=0.78 m, no bubblers, (A) A=25 cm, (B) A=25 cm, (C) A=26 cm.

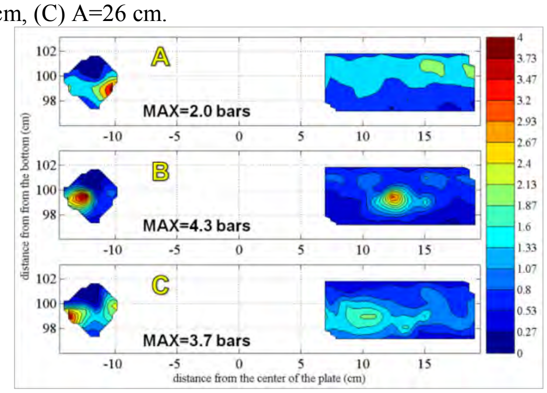

Figure 39 – Soliton cases, pressure evolution, h=0.78 m, no bubblers, (A) A=25cm, (B) A=25cm, (C) A=26cm.

Figure 40 presents the results with the bubbler at location BP3. All the added data in the graph (compared to **Figure 37**) form a dense cloud of points. This is due to the fact that the bubble curtain has little influence on the wave shape as described in subsection "Influence of the parameters of the Soliton generation".

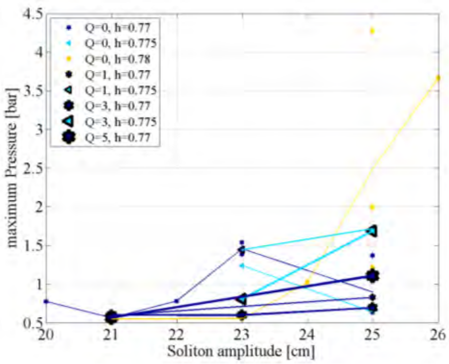

Figure 40 – Soliton cases, evolution of the maximum pressure as a function of the soliton amplitude, the water depth and the air flow rate, bubbler position BP3.

Figure 41 presents the results with the bubbler at location BP1. Here also it has been verified that the bubble flow does not change much the wave shapes for all case tested. Nevertheless, for two tests corresponding to Q_0=3 liters/min and respectively A=21 cm (case (A)) and A=20 cm (Case (B)) relatively high pressures were obtained.

The pressure distribution is presented for these two waves in **Figure 42**. For the case (B), the pressure peak is very localized as previous examples and these high pressures are due to instabilities of the crest. For the case (A) A=21 cm, pressures are more homogeneous and the impact corresponds to a small gas pocket, with a crest slightly destabilized.

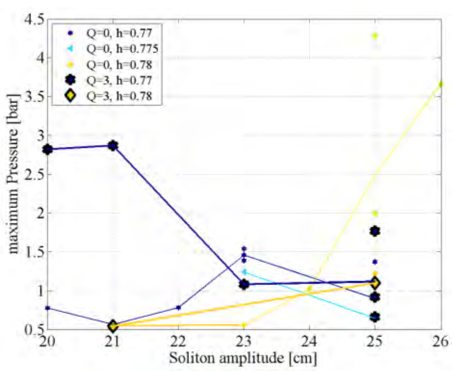

Figure 41 – Soliton cases, evolution of the maximum pressure as a function of the amplitude, the water depth and the air flow rate, bubbler position BP1.

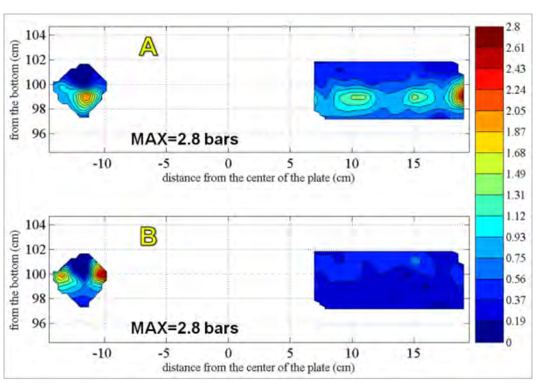

Figure 42 – Soliton cases, pressure evolution, h=77 cm, Q_0=3 l/min, (A) A=21 cm, (B) A=20 cm.

CONCLUSIONS

The principle of a bubble curtain as an anti-sloshing device that could be operated on board LNG carriers has been studied in the wave canal of Ecole Centrale Marseille, in the context of low or partial fillings. Unidirectional breaking waves were generated in order to impact an instrumented wall. Impact loads were compared without and with bubblers at the bottom of the impacted wall. Parameters of the study were related to the wave generation and to the bubblers.

For the wave generation, two principles were used : (1) the focalization technique depending only on the focal distance to the wave maker for a given water depth and a given spectrum of the steering signal ; (2) the generation of a soliton associated to an optimized geometry of a two sloped tank bottom placed in front of the wall. The two parameters studied for this wave generation were both the water depth and the wave amplitude.

For the bubblers, the parameters studied were the types of bubbler (different sizes of bubbles), the distance to the wall and the gas flow rate in a range scaled from values evaluated from a design and an economical perspective. This range is essential to keep in mind as it is clear that without any limit on the gas flow rate to insufflate into the bubblers, any wave could be almost completely damped.

The instrumentation relied mainly on 100 pressure sensors located in the area targeted for the impacts and on three high speed cameras, synchronized with the data acquisition, capturing the last instants of the breaking processes and the impacts.

As stated in the literature, the two main effects induced by bubble curtains are a current and turbulence. The current interacts with waves by slowing down the phase velocity depending on the frequency of the wave components and by filtering the high frequency content of the spectrum. The turbulence adds free surface instabilities to the already existing Kevin-Helmhotz instabilities at the crest level.

- For the wave generation with focalization, these effects express themselves by :
  - A shift of the longitudinal location of the breaking point. The wave starts breaking earlier and the focus is slightly blurred;
  - An even higher variability of the local pressures that could lead sometimes to higher pressures for a same breaking point location ;
  - More localized pressure hot spots on the wall.

  For breaking waves, the highest local pressures are obtained for flip-through types of impacts. Hence, the shift of the breaking point location may lead to Flip-Throughs becoming air-pocket impacts, thus reducing the maximum pressure, but also to slosh impacts becoming Flip-Troughs, thus increasing the pressures.

  The more localized distribution of the loads due to bubble curtains has a real beneficial consequence, as the forces integrating the local pressures on larger areas are always smaller with the presence of bubblers.

- For the wave generation by a soliton and a variable bathymetry in front of the wall, the wave-current interaction is not very strong and the shapes of the waves are almost unchanged. It is understandable because the frequency content of the soliton is very narrow and almost not concerned by the phase velocity shift or the low-pass filtering. On the other hand, the highest variability of the local pressures and the smaller size of the high loaded areas are still observed.

These results made GTT draw the conclusion that the principle of bubble curtains is not relevant for developing an anti-sloshing device on board membrane LNG carriers.

REFERENCES

Brennen, CE, (1995), "Cavitations and Bubble Dynamics", *Oxford University Press*, Oxford.

Brosset, L, Mravak, Z, Kaminski, M, Collins, S, and Finnigan, T, (2009), "Overview of Sloshel Project", *Proceedings of 19th International Offshore and Polar Engineering Conference*, Osaka, Japan.

Bulson, PS, (1968), "The theory and design of bubble breakwaters", *Proceedings 11th International Conference on Coastal Engineering,* London, Volume 2, pages 995-1015.

Drazin, P. G. and Reid, W. H., (2004), "Hydrodynamic stability", *Cambridge University Press*, 2004.

Evans, JT, (1955), "Pneumatic and similar breakwaters", *Proc. R. Soc. Lond. A,* Volume 231, pages 457-466.

Guizien, K and Barthelemy, E, (2002), "Accuracy of solitary wave generation by a piston wave-maker", *journal of hydraulic research*, volume 40, number 3, pages 321-331.

Hensen, W, (1957), "Modelversuche mit pneumatischen Wellenbrechern," *Mitteilungen der Hannover'schen Versuchsanstalt für Grundbau und Wasserbau*, Franzius-Institut der TU Hannover, pages.179-214.

Kaminski, M.-L and Bogaert, H, (2009), "Full scale sloshing impact tests", *Proceedings of 19th International Offshore and Polar Engineering Conference*, Osaka, Japan.

Kimmoun, O, Ratouis, A and Brosset, L, (2010), "Sloshing and scaling: experimental study in a wave canal at two different scales," *20th Int. Offshore and Polar Eng. Conf.*, Beijing, China, ISOPE.

Kobus, H.E., (1968), "Analysis of the flow induced by air-bubble systems", *Proceedings of the 11th Conference on Coastal Engineering*, London, vol. 2, pp. 1016–1031.

Kurihara, Michinori, (1955-1958), "On the Study of a Pneumatic Breakwater", appears in five parts in *Reports of Research Institute for Applied Mechanics, Kyushu University*, 1955-58.

Lafeber, W., Brosset, L., Bogaert, (2010), "Elementary Loading Processes (ELP) involved in breaking wave impacts: findings from the Sloshel project", *22th (2012) Int. Offshore and Polar Eng. Conf.*, Rhodos, Greece, ISOPE.

Laurie, AH, (1952), "Pneumatic breakwaters", *Dock and Harbor Authority,* 33.

Preissler, G, (1960), "Wellendämpfung durch Pressluft", *Wasserwirtschaft-Wassertechnik,*10. Jahrgang, Helft 11: pp. 514-519, Helft 12: pp.560-567.

Puleo, J.A., Johnson, R.V. and Konney, T.N., (2004), "Laboratory air bubble generation of various size distributions", *Review of scientific instruments*, volume 75, number 11, pages 4558-4563.

Scolan, Y-M, (2010), "Some aspects of the flip-through phenomenon: A numerical study based on the desingularized technique," *Journal of Fluids and Structures*, Volume 26, Issue 6, Pages 918-95.

Scolan, Y-M, (2011), "Propagation of a soliton on a two-planes beach," *Report,* 7 pages.

Temperville, A, (1985) "Contribution à l'étude des ondes de gravité en eau peu profonde", *Thèse d'Etat*, Université Joseph Fourier – Grenoble I.

Zhang CX, Wang, UX, Wang, GY and Yu, LM, (2010), "wave dissipating performance of air bubble breakwaters with different layouts", *Journal of Hydrodynamics,* volume 22(5), pages 671-680.